Rock Salt Oxide Hollow Spheres Achieving Durable Performance in Bifunctional Oxygen Energy Cells

*Po-Chun Liao,[a] Ren-Huai Jhang,[a] Yu-Hsiang Chiu,[a] Joey Andrew A. Valinton,[a] Chia-Hao Yeh,[a] Virgilio D. Ebajo Jr.,[a,b] Ching-Hsuan Wang,[a] and Chun-Hu Chen[a]**

[a]Department of Chemistry, National Sun Yat-sen University, Kaohsiung, Taiwan 80424

[b]Department of Chemistry, College of Science, De La Salle University, Manila 1004, Philippines

Email: chunhu.chen@mail.nsysu.edu.tw

ABSTRACT: Interchangeable operation of alkaline oxygen evolution and reduction using bifunctional electrocatalysts in devices consolidates the commercialization milestone of energy storage in hydrogen, yet usually limited by issues of carbon corrosion in electrocatalysts and inhomogeneous electrode fabrication. Here, we demonstrate a synthetic route toward carbon-free ternary rock salt oxide (i.e. NiO/CoO/FeO) hollow spheres with silver decoration on the surface for durable operation in bifunctional cells. This Ag-decorated ternary oxides exhibit an overall bifunctional potential gap ($\Delta E = E_{j10,\ OER} - E_{jhalf,\ ORR}$) of 0.89 V. The operando Raman studies discover that the rock salt structure shows the phenomena of highly reversible local environment during the charge-discharge OER cycles, a key characteristic for high durability in bifunctional devices. At equivalent content between Ni and Co, NiOOH is the main OER active species with CoOOH and/or CoO_2 as co-catalyst, where the presence of FeO dopant facilitates structural activation and reversibility. On the proof-of-concept performance in anion-exchange membrane (AEM) devices, the catalysts achieve a durable cyclic operation with a high current density (1000 mA cm^{-2}) at smaller potentials (2.03 V) than RuO_2 (2.16 V) under the electrolyzer mode, while it can yield two-times greater power density (96.98 mW cm^{-2}) than Pt/C (53.58 mW cm^{-2}) under fuel cell mode.

Keywords: rock salt, bifunctional cell, carbon-free, oxygen evolution, oxygen reduction, operando Raman

1. INTRODUCTION

Finding scale- and cost-effective storage for intermittent green energy poses the critical challenge for the future commercialization of sustainable energy industry.[1, 2] Highly efficient electrocatalysts active for both oxygen evolution reaction (OER) and oxygen reduction reaction (ORR) in a single cell ideally address the challenge in minimizing device dimensions and fabrication costs in massive-scale power stacks.[3-5] However, interchangeable operation between oxidative OER and reductive ORR significantly decays carbon-based electrocatalysts, such as commercial benchmark Pt/C, where the low-density nature of carbon dots enables excellent dispersion for uniform electrode fabrication.

Mimicking Pt/C by using different dimension carbon supports, such as graphene, suffers from severe aggregation due to 2D nature of sheet structure.[6-8] Because carbon corrodes rapidly under highly oxidative OER, and disintegrates due to thermodynamic instability under ORR,[9] carbon-free strategy becomes a rational design of durable electrocatalysts for bifunctional devices.[3, 10] Metal oxide materials are promising replacement for carbon due to the high stability under alkaline OER conditions, but they are generally too dense to maintain dispersion homogeneity.

Doping impurities in metal oxides is an effective approach to improve conductivity and activities. As such, homogeneous mixing of multiple metals in a single oxide phase enables drastic reduction of the intrinsic electrical resistivity.[10, 11] However, studies show that Co-Ni binary oxides, as highly OER-active species, tend to form separate phases (e.g. NiO and Co_3O_4) at varying Co/Ni ratios.[12] We proposed to utilize rock salt oxide as the common structure to incorporate Co and Ni into a single phase with identical local environment.[13, 14] An enhanced intrinsic conductivity and structure stability in cyclic,

bifunctional electrocatalysis are anticipated. Although rock-salt oxides of Ni and Co solid solution was known for more than half a century,[15] their bifunctional purpose has not been well recognized.

Our rational approach involves constructing OER-active rock salt oxide spheres with hollow structure aiming to lower the density and enhance dispersion homogeneity (see Scheme 1). Analogous to Pt/C, we substitute more affordable Ag instead of Pt on the sphere surface to gain ORR activity. Studies show that the heterojunction between silver and metal oxides can balance adsorption and desorption kinetics of oxygen, an essential property to achieve comparable ORR kinetics to Pt.[16, 17] Moreover, to further improve OER activity, the as-prepared NiO-CoO rock salt oxides serve as a structure-directing matrix to stabilize Fe dopant as rock salt FeO, rather than other thermodynamic-favored phase (e.g. hematite). To understand the local structure dynamics of the as-yield ternary rock salt oxides, the operando Raman spectroscopy reveals a highly reversible local coordination under charge-discharge OER cycles, a desired characteristic to benefit durable device operation. The anion exchange membrane (AEM) cells perform repetitive fuel cell-electrolyzer interchange functionality without significant decay in current density and electrochemical impedance. In addition, the rock salt hollow sphere composites exhibit superior electrolyzer and fuel cell performance to benchmarks (RuO_2 and Pt/C). The combined strategy of carbon-free hollow sphere and ternary rock salt oxide is highly effective to achieve bifunctional cell operation with great durability.

2. RESULTS AND DISCUSSION

2.1 Synthesis of silver-decorated NiO-CoO hollow spheres

The NiO-CoO hollow spheres (NCO-HS) were first prepared by a two-step procedure (see Supporting Information for the details)[8, 16] The SEM images (Figure 1a) reveal that the NCO-HS exhibits uniform spheres with diameters of 150–200 nm and smooth surface.[18] The TEM images (Figure 1b) confirm the presence of a hollow core in NCO-HS with the shell thickness of 30–45 nm, as well as the absence of other impure structures. To decorate Ag nanoparticles on the surface of NCO-HS, we utilized (3-aminopropyl)trimethoxysilane (APTMS) to functionalize the surface with terminal amine groups for coordination with Ag^+, which was further reduced by refluxing in DMF.[19] The entire synthesis is summarized in Figure S1a. As shown in Figure 1c-d, Ag nanoparticles (17.28 ± 7.69 nm, Figure S1b) were observed attaching on the surface, while the hollow-core structures remained intact. The EDS elemental mapping (Figure 1g) confirms the homogeneous distribution of Ni (green) and Co (red) in the shell, while the Ag signals (blue) are shown on particles decorated around the Ni/Co oxide shell. This agrees with the high resolution (HR) TEM images (Figure 1e) indicating that the decorated particles contain a lattice fringe of 0.235 nm corresponding to Ag (111). The atomic ratios of Co to Ni are nearly one and in agreement with the equivalent amounts of the precursors in the reaction mixture (Figure 1g, Figure S2).

Although the XRD patterns of NCO-HS correspond to rock salt NiO and CoO (Figure 1f), the significant peak broadening results in the difficulty of exclusive phase identification.[19] The small deviations among their characteristic peaks are due to the difference in their unit cell parameters caused by the unequal ionic radii (i.e. Ni^{2+} and Co^{2+}

are 0.72 Å and 0.69 Å, respectively).[20] Thus, we further studied the crystallinity evolution of NCO-HS at various temperatures in air (Figure 2). No observable change in the pattern occurred at lower temperatures until at 300ºC, where additional peaks at 2θ of 59.46° and 65.13° appear prominently due to increased crystallinity. At 500-700ºC, the diffraction peaks emerge at 31.31º, 36.92º, 44.85º, 59.46º, and 65.13º corresponding to the crystal indices of Co_3O_4 at (220), (311), (400), (511) and (440), respectively. By 700-800ºC, Co_3O_4 phase starts to transform into the fcc CoO phase, and eventually becomes fcc NiO phase at 900ºC. In retrospect, this observed temperature-dependent crystal phase evolution is highly consistent with the earlier report on rock-salt NiO-CoO,[13] further confirming that the synthesis of NCO-HS becomes a rare example of directly producing nanocrystalline NiO-CoO solid solution at low temperatures (< 200ºC), compared to these at 800ºC.[13]

The elemental compositions of NCO-HS and Ag/NCO-HS were investigated by X-ray Photoelectron Spectroscopy (XPS). (Figure S3) In NCO-HS, the divalent state of Ni^{II} and Co^{II} is confirmed based on the observed binding energies of Ni [Ni $2p_{3/2}$ at 854.3 eV (satellite peak at 860.0 eV) and $2p_{1/2}$ at 872.3 eV (satellite peak at 878.4 eV) (Figure S3a)],[21] and of Co [Co $2p_{3/2}$ at 779.6 eV (satellite peak at 784.8 eV) and $2p_{1/2}$ at 795.4 eV (satellite peak at 801.6 eV), with a peak difference of 15.8 eV (Figure S3b)][22], respectively. These agree with rock-salt NiO-CoO phase in the XRD data. In the case of Ag/NCO-HS, the binding energy of NiO and CoO shifts higher by 1.2 eV and 1.4 eV, respectively, as compared to NCO-HS; while XPS signals of silver at 367.8 eV ($3d_{5/2}$) and 374.0 eV ($3d_{3/2}$) are lower by 0.4 eV than typical values reported in the literature (Figure S3c).[23] Such the observations are the result of inhomogeneous distribution of electron density associated with the presence of metal/metal oxide heterojunction site. The binding energy shifts

suggest the polarization of the interactions between Ni^{2+}/Co^{2+} and Ag. The increased cationic character in Ni^{2+} and Co^{2+}, based on theoretical XPS studies, [24] facilitates their conversion to higher valence states as active OER species by Ag decoration.[25] In an earlier study on Ag@$Co(OH)_2$, observed higher XPS shifts in Co^{2+} affected by Ag decoration became correlated with the electron deficiency of the former, according to theoretical models.[26] Consequently, Ag becomes an electron acceptor, which also promotes electron transfer in ORR. [27] Such compartmentalization of species with a lowered binding energy as ORR active and otherwise as OER active has been displayed on various metal-metal oxide heterojunction materials.[27-30] In this manner, the heterojunction created by the Ag addition can result in the enhancement of the reactions catalyzed by each component.

To understand the roles of oleylamine and TBAOH in hollow structure formation, the control experiments of oleylamine-free and TBAOH-free syntheses were carried out. In the absence of oleylamine, spherical shapes with solid-core characteristics (denoted as NCO-SC) form, according to the SEM and TEM images (Figure 3a, c), indicates that oleylamine may serve as soft template for hollow structure formation.[31] Meanwhile synthesis in the absence of TBAOH results in irregular, fine particles (<15 nm Figure 3b, d). By suspending equal masses of either hollow-core or solid-core samples in water (Figure 3e), the suspensions of former (NCO-HS and Ag/NCO-HS) remain homogeneous over 24 hours, while the latter turned otherwise. Thus, the low-density hollow structure to acquire high dispersion ability is well justified.

2.2 Electrocatalytic oxygen evolution

The OER performance of the prepared catalysts was evaluated by linear sweep voltammetry (LSV) under O_2-saturated 0.1 M KOH (Figure 4a-b). NCO-HS exhibits a lower onset potential at 1.45 V than NCO-SC (1.49 V), and smaller overpotential (η at 10 mA cm^{-2}) of 360 mV than 422 mV of NCO-SC. The hollow structure of NCO-HS possibly enables efficient mass transport,[32, 33] resulting to greater OER activity than the solid-core samples.

As compared to NCO-HS, Ag/NCO-HS exhibits a more superior OER activity with a lower onset potential (1.40 V) and overpotential (310 mV). No obvious OER activity is observed in the LSV of pure Ag nanoparticles, revealing that the NiO-CoO surface mainly acts as the OER-active sites. In comparison, Ag/NCO-HS shows higher performance than commercial OER benchmark RuO_2 (onset potential of 1.42 V and η of 340 mV), and a high OER stability with negligible decay after 1000 sweeping cycles (Figure S4). Long-term durability tests of Ag/NCO-HS at a constant potential (1.63 V) exhibits 98% retention of its original current after 24 hours, while RuO_2 retains only 23% showing massive decay (Figure S5). After the durability test, SEM images of Ag/NCO-HS show insignificant morphological change and hollow structure retention (Figure S6). The corresponding ICP-MS analyses of the electrolyte solution post-experiment reveal a small amount of element leaching from Ag/NCO-HS (i.e. less than 0.5 mol %, see Figure S6), suggesting a promising retention of structural integrity as compared to 20-30% leaching of the reported CoO_x and $CoFeO_x$ within 6 hours.[34] Elevated OER potentials generally lead to a higher probability of structure distortion/defects to occur. Due to that, the much faster cycles of bond breaking and re-formation can cause irreversible alteration in coordination structures.

Oxygen bubbling is also a strong force to detach Ag from the hollow sphere surface. The selected OER potential ranges enable a high catalytic conversion and bubble formation without putting excessive electrocatalytic stress that can compromise the hollow structure, as well as the attachment of Ag.

The presence of high oxidation states of the metal cations is essential to promote OER performance. The oxidation of $Co^{II} \rightarrow Co^{III}$ and $Ni^{II} \rightarrow Ni^{III}$ in the corresponding mono-metal oxide is around 1.15 V and 1.45 V, respectively.[14, 35] The shift of $Ni^{2+/3+}$ transition (in voltage) toward the lower potentials (i.e. 1.33-1.35 V in Figure 4b) is associated with the coexisting of Co and Co/Ni ratios in the rock salt oxides. The stronger intensity of $Ni^{2+/3+}$ peak in the hollow structure samples (NCO-HS) than the solid core ones (NCO-SC) suggests the more coverage of accessible Ni^{3+} sites because the thin shell of hollow spheres allows more facile activation than the impermeable cores (also see ECSA study below).[36]

After Ag decoration, the LSV of Ag/NCO-HS (Figure 4b) shows two separate oxidation signals at 1.15 V (yellow band) and 1.35 V (blue band). The first peak (red star-labeled) corresponds to Co^{2+}/Co^{3+} transition,[14, 37] which means that Ag decoration stimulates Co activation compared to the Ag-free samples. The intense overlapping transitions between these two signals may suggest a sequential interaction starting from Co activation towards the Ni oxidation, contrary to an earlier report on the Co-inhibited transition of NiO to oxyhydroxide in the absence of Ag.[14] Despite the poor catalytic activity of standalone Ag particles, the OER enhancement delivered by Ag decoration on the rock salt oxides is consistent with the altered electronic structure at the heterojunction sites according to XPS data above. This also implies a new activation pathway of this rock salt oxide-based composites.

In terms of OER kinetics, Tafel plots (Figure 4c) show that NCO-HS (68 mV/dec) has superior kinetics compared to NCO-SC (96 mV/dec) due to the performance associated with hollow structures.[38] Meanwhile, Ag/NCO-HS gives the lowest Tafel slope (60 mV/dec), comparable to benchmark RuO_2 (62 mV/dec), showing that the Ag-decorated solid solution can reach OER kinetics similar to the benchmark. The electrochemical surface area (ECSA) comparison of these samples is shown in Figure S7. The ECSA of the hollow sphere samples, Ag/NCO-HS (23.7) and NCO-HS (20.6), is higher than NCO-SC (12.5) by 90% and 65%, respectively. The interior shell of hollow structure provides more electrocatalytic active sites[32] than the solid core samples, consistent with OER activity trend (Figure 4a) where the presence of a hollow structure shows an increase in OER electrocatalytic performance.

In terms of mass activity (at η = 350 mV), Ag/NCO-HS (489 A/g) is 3.85 times higher than benchmark RuO_2 (Table S1). Meanwhile, its turnover frequency (TOF) (0.109 s^{-1}) is higher than that of RuO_2 (0.0347 s^{-1}). Due to the Ag decoration, it has a higher mass activity (8.15 times higher) and TOF (9.4 times higher) than the silver-free sample (NCO-HS).

2.3 Electrocatalytic oxygen reduction reaction

The ORR performance of NCO-HS shows its onset potential at 0.68 V with two-step LSV curves corresponding to two-electron reduction (Figure 4d), commonly observed in transition metal oxide electrocatalysts.[8, 16, 39] A two-step ORR usually leads to the release of hydrogen peroxide (HO_2^-), which is highly corrosive to catalysts and the fuel cell

membrane. Thus, a single-step ORR with a four-electron transfer is preferred. In comparison, Ag/NCO-HS shows a more positive onset potential (0.83 V) than NCO-HS, and a one-step LSV curve with higher current density. The LSV change from two-step to one-step curve indicates that the silver decoration enables a four-electron reduction. Also, the presence of plateau currents of Ag/NCO-HS around 0.3 V reveal a similar equilibrated oxygen adsorption and OH^- desorption kinetics to ORR by benchmark Pt/C. Compared to pure Ag nanoparticles in Figure 4d, the onset potentials of Ag/NCO-HS become slightly more positive, suggesting that the Ag, influenced by the rock salt oxide through the heterojunction interface, mainly contributes to the ORR activity.[16]

The electron transfer number values (*n*) are presented in Figure S8. Ag/NCO-HS exhibits the greatest and most complete *n* value of 3.9 stretched over a wide potential range of 0.20-0.65 V; while NCO-HS only shows incomplete reduction with an *n* value close to 2 at around 0.6 V. The corresponding HO_2^- yields of NCO-HS and Ag/NCO-HS are at 20% and 5% at 0.5 V, respectively (Figure S9), confirming that decorating Ag influences a complete, four-electron route and the inhibition of HO_2^-.[40] The electrochemical impedance spectroscopy (EIS) has shown that Ag decoration decreases the charge transfer resistance to allow improved kinetics and the electrocatalytic performance (Figure S10).[16] Methanol crossover [41], which can potentially poison ORR catalysts in direct methanol fuel cells, can be tolerated by Ag/NCO-HS (see the details in Figure S11).

2.4. Fe doped oxides

To further improve the OER activities of Ag/NCO-HS, a small amount of iron was introduced.[42, 43] The iron oxide-doped NiO-CoO hollow spheres (denoted as FNCO-HS) were synthesized by adding the iron precursor in the first step of reflux (before the base addition), followed by the Ag decoration to yield Ag/FNCO-HS. The TEM images (Figure 5a) show similar morphologies to the binary Ag/NCO-HS with uniform Ag particle distribution. The XRD patterns (Figure S12) also show the nearly identical phase to Ag/NCO-HS, suggesting no significant alterations in the rock salt structure due to iron oxide doping. In fact, reports show that Ni and Co oxide solid solutions stabilize the homogeneously contained Fe.[35, 43] The EDS mapping (Figure 5b) shows that all three metals are evenly dispersed in the hollow spheres while Ag is decorated on the outer surface. The ICP-MS (Table S2) shows 9% Fe doping in Ag/FNCO-HS. With the hollow-core structure, Ag/FNCO-HS retains suspension homogeneity, similar to Ag/NCO-HS, for at least 24 hours (Figure 3e).

In comparison with the non-doped variant, the iron-doped samples show the improved OER activities (i.e. 10% decrease in overpotential, Figure 5c), while the ORR onset potential has no significant change (Figure S13) under the identical Ag content (Table S2). In the magnified LSV curve (inset of Figure 5c), the intensity of $Ni^{2+/3+}$ transition peak at 1.35 V in Ag/FNCO-HS is much higher than the iron-free counterpart. Such enhancement in Ni activation is similarly observed on Fe^{2+}-added Ni^{2+}/Fe^{3+} layered double hydroxides,[44] yet contrary to the instance of incorporating Fe^{3+} in NiOOH.[43] Although the incorporated surface Fe^{3+} on nickel (or cobalt) oxyhydroxides was recognized as a key active site for OER,[42, 43] we hypothesize that Fe^{2+}somehow retains its oxidation state and aids in

activating Ni^{2+}. Sun et. al. recognizes that the lowered overpotential of promoting $Ni^{2+}$to higher valence states, which can be extended to a larger activated population, is due to the interaction of neighboring $Fe^{2+}$with adjacent Ni^{2+}; [44] but the amount of Fe^{2+}must be kept at a minimum, which is highly consistent with the Fe-doped sample in this study. The overall bifunctional performance of a catalyst for ORR and OER can be evaluated by the potential gap between ORR half wave potentials and OER overpotentials at a current density of 10 mA cm^{-2} ($\Delta E = E_{j10,\ OER} - E_{jhalf,\ ORR}$).[45] An electrocatalyst possessing a lowered electrocatalytic barrier should have a smaller ΔE value.[46] In the case of Ag/NCO-HS, the ΔE was measured to be 0.93 V (Figure 5d) which is generally smaller than the reported carbon-free bifunctional electrocatalysts (see Table S3). After the Fe-doping treatment, the bifunctional ΔE of Ag/FNCO-HS decreases further by 40 mV to Ag/NCO-HS (Figure 5d). Hence, we used the most active Ag/FNCO-HS as the main electrocatalyst for the bifunctional device studies.

2.5 Operando Raman Spectroscopy

To understand the phase transformation (i.e. phase, valences) at varied potentials of OER in the rock salt oxides, we conducted the operando Raman study. Under the dry conditions, Ag/NCO-HS (Figure 6a, green curve) exhibits a broad band at 550 cm^{-1} that corresponds to the Co^{II}-O vibrations (the blue highlight),[47, 48] and a weak band at 670 cm^{-1} associated with the octahedral-coordinated Co^{II}-O stretch (the yellow highlight).[48, 49] NiO has a sole band at 550 cm^{-1} corresponding to Ni^{II}-O bonds, overlapping with that of Co^{II}-O vibrations.[50, 51] For Ag/FNCO-HS (Figure 6a, red curve), the band at 670 cm^{-1} intensifies

more than Ag/NCO-HS due to the octahedral Fe^{II}-O vibrations falling on the same position as the octahedral-coordinated Co^{II}-O stretch.[48, 49]

Immersing Ag/NCO-HS into 0.1 M KOH (Figure 6a, blue curve) results in a depletion of the Co^{II}-O stretch at 670 cm^{-1}, presumably due to the conversion of rock salt oxide into hydroxide structure, although a supposedly Co^{II}-OH vibration of $Co(OH)_2$ at 450 cm^{-1} (pink highlight) remains insignificantly present.[48, 52] The common peak of NiO/CoO exhibits a slight blue shift from 550 cm^{-1} to 560 cm^{-1} also corresponding to this structure transformation.[53] On the other hand, immersion of Ag/FNCO-HS in 0.1 M KOH (Figure 6a, black curve) causes the intense peak at 670 cm^{-1} to nearly flatten with an appreciable rise of the M^{II}-OH at 450 cm^{-1} (M=Co and Fe, the pink highlight).[54] These results further confirm the transformation of rock salt oxide to hydroxide, which is significantly enhanced in the presence of Fe^{II} dopant. In addition, Fe^{II}-OH has signal on 550 cm^{-1} that supplements to the Ni^{II}-O/Co^{II}-O signals, leading to the inappreciable peak shift on the 550 cm^{-1} band, as compared to Ag/NCO-HS.[54]

The potential-dependent phase transformation under OER charging from the rest (at 0.865 V) to OER conditions (at 2.265 V) was shown in Figure 6d and e, where the fully charged active species are both indexed as MOOH (M=Co^{3+} and Ni^{3+}). At the charged state, the strong band at 470 cm^{-1} together with the relatively weak one at 550 cm^{-1} corresponds to the presence of NiOOH.[55-58] Meanwhile, the shoulder at around 600 cm^{-1} (black arrow in Figure 6d), corresponding to Co^{III}-O vibrations in CoOOH,[56, 59] shows up coinciding with the NiOOH peaks. Another peak also corresponding to CoOOH at ~500 cm^{-1} is unobservable due to the overshadowing of NiOOH signals. The oxidation of Co^{III}OOH to $Co^{IV}O_2$ at the elevated potentials is difficult to identify exclusively, due to a small peak

shift and the strong overshadowing signals from NiOOH.[59] As Co and Ni are both half-occupying all the octahedral sites (i.e. Ni/Co = ~1), their phase transformation should be strongly influenced by common structure effect of oxyhydroxide.

In comparison, the operando Raman curves of Ag/FNCO-HS (Figure 6e) are similar to those of Ag/NCO-HS at the fully charged conditions, except the slightly band broadening due to the structural incorporation of FeO impurity.[60] The Raman data also show earlier activation at 1.265 V (Figure 6e, green) than the iron-free electrocatalysts at 1.365 V (Figure 6d, cyan), where the signal at 470 cm^{-1} starts to arise. In addition, iron oxyhydroxide signal at 675 cm^{-1} is absent at 1.865 V (Figure 6e, black). These results collectively suggest that the iron dopants promote the NiOOH/CoOOH activation, rather than forming FeOOH to participate OER electrocatalysis as reported by Niu et al.[61] The corresponding LSV (Figure 5c) reveals the higher population of $Ni^{2+/3+}$ activation in the presence of iron, further supporting the role of iron in lowering the structural transformation barrier. A small amount of Fe^{2+} doping could stabilize the high-valent state of Ni sites and thus decrease the activation potentials[44]. As such, the extensive $Ni^{2+/3+}$ conversion suggests that NiOOH is the major active sites for OER, while CoOOH and/or CoO_2 act as a co-catalyst.

Long-term stability of electrocatalysts depends on the reversibility of phase transformation in cyclic charge/discharge operation. We thus monitored Ag/FNCO-HS from the rest condition (Figure 6b, black curve) to fully charged status at 2.365 V (Figure 6b, green), and then discharged the electrocatalysts immediately back to the rest conditions (Figure 6b, red) as a complete charge/discharge cycle. After repeating this process for several times (Figure 6c), the discharged state shows the three characteristic bands at 450

(red band), 550 (blue band), and 670 cm^{-1} (orange band) similar to the fresh electrocatalysts before any tests, indicative of a high structural reversibility in OER. This reversible transformation suggests the octahedral coordination units (M=Co, Fe, and Ni) of rock salt structure are not significantly altered during the charging/discharging process.

Rock salt structure is entirely comprised of octahedral (MO_6) units, which should minimize transformation barrier, in contrast to mixed local environments. Mixed coordination of octahedral (MO_6) and tetrahedral (MO_4) sites in spinel oxides (also recognized as a widely reported OER-active phase in the literature, such as Co_3O_4) could increase the barrier of structural reversibility and probability of deconstructive transformation after the cyclic OER operation. The difference between crystal field stabilization energies (CFSE) of low-spin $Co^{2+}{}_{Oh}$ ($t_{2g}{}^6e_g{}^1$) to $Co^{3+}{}_{Oh}$ ($t_{2g}{}^6e_g{}^0$) is only $3/5\Delta_{Oh}$ (without counting pairing energy), much lower than the energy required to oxidize $Co^{2+}{}_{Td}$ to $Co^{3+}{}_{Td}$. Likewise, metal oxidation in a T_d environment of spinel oxides can be less energy favorable than a sole O_h environment.[49] Intersystem coordination rearrangement between O_h and T_d systems can be even more energy unfavorable.

The reversible structural transformation of the rock salt oxides, according to the data above, is illustrated in Scheme 2. The dashed line aligns the metal cation layer among phases of rock salt, metal hydroxides, and metal oxyhydroxides. One can find that migration of metal cations to other position or layers is not required upon phase transformation, as all the metal cations sit in a six oxygen-coordinated environment solely (no T_d sites). The structure alteration only occurs at the changes of interlayer d-spacing due to electrolyte interactions. These characteristics rationalizes a reliable structural

reversibility during the rapid cyclic OER tests with Ag/FNCO-HS. These unique rock salt-enabled characteristics are essential criteria for durable performance of bifunctional cells.

2.6 Device performance

The bifunctional performance was evaluated in an anion exchange membrane (AEM) device under electrolyzer (OER) and fuel cell modes (ORR), as shown in Figure 7a. Ag/FNCO-HS requires a lower potential (2.03 V) than the benchmark RuO_2 (2.16 V) to reach a current density of 1000 mA cm^{-2} (Figure 7b), agreeing with the three-electrode measurement where Ag/FNCO-HS requires a lower OER overpotential (η= 282 mV) than RuO_2 (η = 340 mV). In terms of bulk electrical conductivity of the electrocatalysts has a critical influence on device performance,[62, 63] the measured bulk electrical conductivity of Ag/FNCO-HS (1.1 x 10^{-1} S cm^{-1}) and RuO_2 (2 x 10^{-1} S cm^{-1}) possesses comparable values. The greater electrolyzer performance of Ag/FNCO-HS than RuO_2 is most likely due to the intrinsic electrocatalytic activities, rather than conductivity effect. On testing the stability with a relatively high current density (~200 mA cm^{-2}) at 1.5 V for 3 hours,[62] Ag/FNCO-HS shows higher durability (<0.1% decay) compared to RuO_2 (5.5% decay) (Figure 7c). The EIS of Ag/FNCO-HS device shows no obvious change after stability test (inset of Figure 7c), while the charge transfer and mass transport resistances of RuO_2 cell apparently increased. The current decrease of RuO_2 cell may be due to passivation/dissolution or any potential irreversible phase transformation of electrocatalysts.

The AEM fuel cell functionality was tested with the same cell assembly above but changing the flow direction of H_2 and O_2, as indicated in Figure 7a. We fabricated the reference devices utilizing benchmark Pt/C as the ORR electrocatalyst for comparison. As

shown in Figure 7d, Ag/FNCO-HS shows a higher open circuit voltage (OCV) of 0.90 V than Pt/C (0.81 V), and exhibiting the higher working potentials than Pt/C device at various current densities (Figure 7d, the curves of red squares and black dots). Ag/FNCO-HS indeed possesses a lower activation energy barrier than Pt/C.[48, 49] At the targeted current output (i.e. 44 mA cm^{-2} for platinum group-free fuel cells),[50] Ag/FNCO-HS shows a higher potential (0.66 V) than the Pt/C device (0.61 V). Moreover, the maximum power density of Ag/FNCO-HS device is 96.98 mW cm^{-2}, almost two-times higher than the Pt/C devices (the hollow red square and open-dot curves in Figure 6d), suggesting that Ag/FNCO-HS allows better energy conversion than Pt/C.

Notably, the performance of Ag/FNCO-HS is greater than Pt/C in the real device conditions but reverse in ideal three electrode system. The accessible exposure of catalyst to electrolyte ions (OH^-) in a real device is mainly governed by its junction interface with AEM membrane. This factor cannot be incorporated in a three electrode system, as the catalyst experiences full liquid electrolyte exposure. In Pt/C, the irreversible Pt-catalyzed corrosion of carbon hampers the ion transport due to the impaired junction interface which significantly decays the ORR performance in a device despite its high performance in the three-electrode system.[64, 65] As such, the carbon-free Ag/NCO-HS avoids the junction impairment between catalysts and AEM, causing the better ORR performance than Pt/C in fuel cell mode. In the stability test of the fuel cell mode at a constant current density of 100 mA cm^{-2},[66] the Ag/FNCO-HS cell shows a higher stability with only 0.1% decay, compared to Pt/C fuel cell (10.9% decay) after a 3-hour test (Figure 7e). The relatively large decay in Pt/C may come from the typical electrochemical corrosion of carbon component.[9]

To evaluate the interchangeable performance, the device was first conducted

electrolyzer mode with Ag/FNCO-HS on the oxygen-evolution electrode, followed by switching to fuel cell mode with O_2 going through the Ag/FNCO-HS electrodes. Switching from electrolyzer to fuel cell modes is considered as one complete cycle. After a 10-cycle test, the Ag/FNCO-HS electrodes show the nearly identical bifunctional performance (Figure 8a), while Pt/C-based oxygen-evolution electrode in a reference device reveals a significant electrolyzer decay by losing 61.1% current density (at 1.5 V) and fuel cell decay by losing 80.6% that (at 0.5 V). To quantify the bifunction efficiency, the ratios between the potentials obtained in both fuel cell and electrolyzer modes are calculated as round-trip efficiency which is described by the following equation:[3]

$$\text{Round-trip efficiency} = \frac{V_{\text{fuel cell}}}{V_{\text{electrolyzer}}} \times 100\% \qquad [1]$$

where $V_{\text{fuel cell}}$ is the potential generated at 100 mA cm^{-2} in fuel cell mode; and $V_{\text{electrolyzer}}$ is the potential required to reach 100 mA cm^{-2} in electrolyzer mode.

The $V_{\text{electrolyzer}}$ of Ag/FNCO-HS devices required 1.40 V in water splitting and generated electricity of 0.52 V as fuel cell. Thus the devices receive a round-trip efficiency of 37.1% in its first cycle, and remain the same after in the tenth-cycle (Figure 8b).[3] In contrast, carbon-based Pt/C shows the round-trip efficiency of 31.4% in the first cycle but gradually decreases to 2.4% in the tenth cycle due to carbon corrosion.[3] The carbon-free nature of Ag/FNCO-HS avoids decay in carbon components during anodic OER conditions;[67, 68] resulting to high robustness under electrolyzer-fuel cell cycling (Figure 8c). The structural reversibility also aids the long-term durability for device applications.

3. CONCLUSION

We successfully demonstrated highly dispersible, carbon-free electrocatalysts based on ternary rock salt oxides exhibiting durable performance in bifunctional AEM devices. The exceptional device performance of Ag/FNCO-HS as compared to benchmarks of Pt/C and RuO_2 has been accomplished. The carbon-free nature eliminates the corrosion issue; the hollow structure preserves suspension ability; and the homogeneous rock salt oxides create a new route of achieving structural reversibility and durability even under the harsh conditions of cyclic tests. Our Raman study confirms the key characteristic of highly reversible structure and iron-promoted phase transformation responsible for the exceptional bifunctional performance. Further adjustment of elemental ratios in multinary rock salt oxides is therefore anticipated to optimize the device performance in future studies. Rapid and simplified syntheses towards metal/metal oxide hollow spheres are also needed to truly achieve massive-scale applications.

ASSOCIATED CONTENT

Supporting Information. Experimental procedures, synthetic procedure scheme, embedded Ag particle size histogram, characterization data (EDS, XPS), OER stability tests, electrochemical surface area, ORR electrochemical data (electron transfer number, hydrogen peroxide yield, electrochemical impedance, and methanol crossover), iron doping comparisons (XRD, ORR LSV, and ICP-MS data), and comparison tables (versus benchmarks and other catalysts in literature).

The following files are available free of charge.

Supporting Information File (PDF)

AUTHOR INFORMATION

Corresponding Authors

*chunhu.chen@nsysu.edu.tw (C.-H. Chen)

Author Contributions

The manuscript was written through contributions of all authors. All authors have given approval to the final version of the manuscript.

ACKNOWLEDGEMENT

We acknowledge the financial support from Ministry of Science and Technology, Taiwan under grant 108-2113-M-110-002, and the New Southbound Project of

Academic Alliance supported by Ministry of Education, Taiwan. We also thank Prof. Steven Suib for the help on electron microscopy.

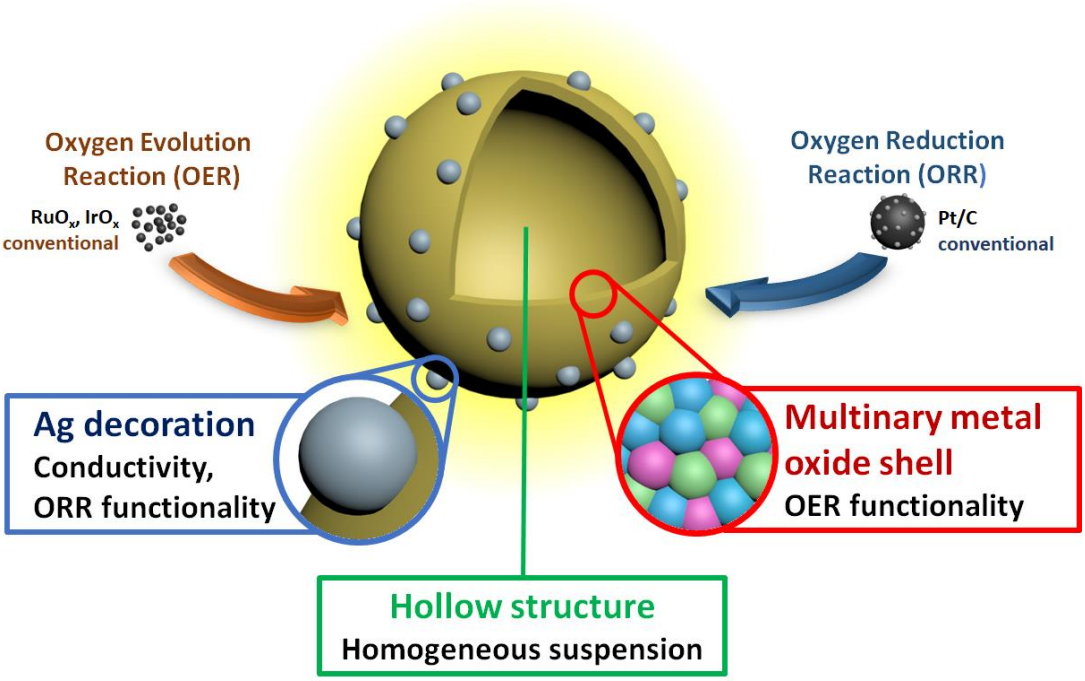

Scheme 1. The design concept of carbon-free bifunctional electrocatalyst. The multinary rock salt oxide shell (NiO, CoO, and FeO) is responsible for oxygen electrochemical evolution functionality (before the OER activation), instead of using Ru- and Ir-based oxides. Ag decoration on the shell aims to mimic the role of Pt in Pt/C for ORR functionality. The hollow structure affords a lowered density to achieve a reasonable dispersion capability.

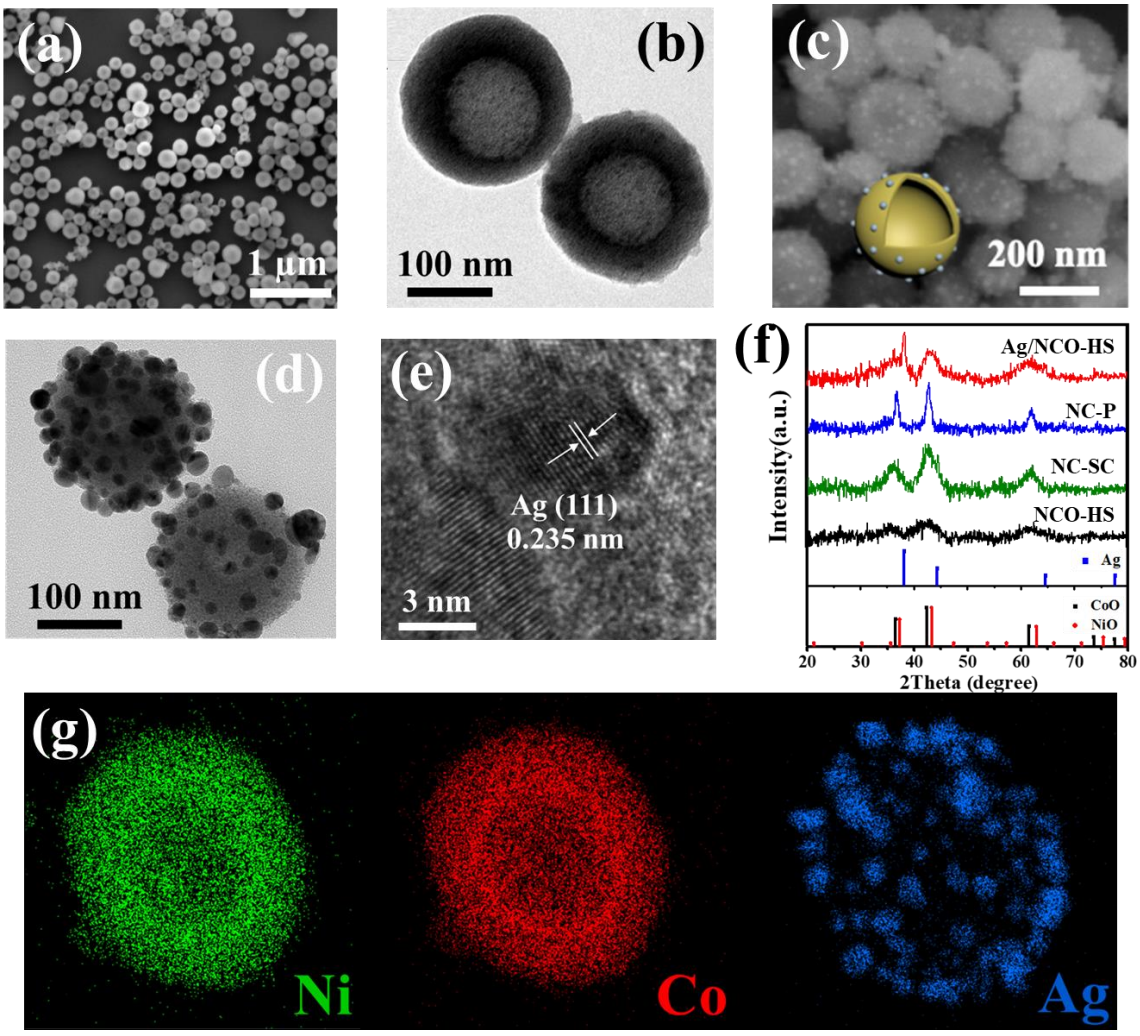

Figure 1. Characterization of the prepared rock salt oxide spheres. (a) SEM and (b) TEM images of NiO-CoO hollow spheres (NCO-HS). (c) SEM and (d) TEM images of Ag-decorated NCO-HS (Ag/NCO-HS). (e) HR-TEM image of Ag/NCO-HS showing the lattice fringes pertaining to Ag. (f) XRD patterns of Ag/NCO-HS, NCO-HS, powdered NCO (NCO-P) and solid-core NCO (NCO-SC). (g) EDS mapping of Ni, Co and Ag of an individual Ag/NCO-HS sphere.

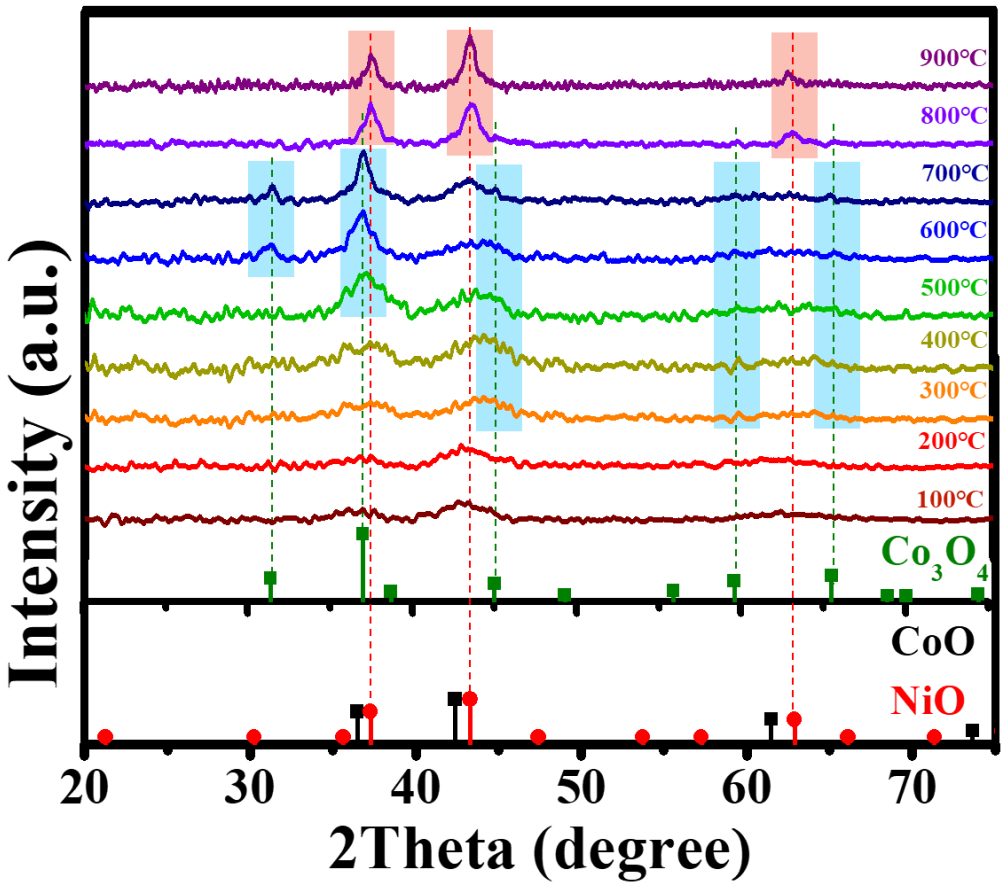

Figure 2. The phase transformation of NCO-HS monitored by XRD at calcination temperature range from 100-900ºC. Co_3O_4 phase occurs from 300ºC, then disappeared in 800ºC (see the blue bar labels). The co-existing NiO and Co_3O_4 phases turns into a single phase as the temperature reaches 800ºC, corresponding to rock salt CoO-NiO solid solution of NCO-HS.

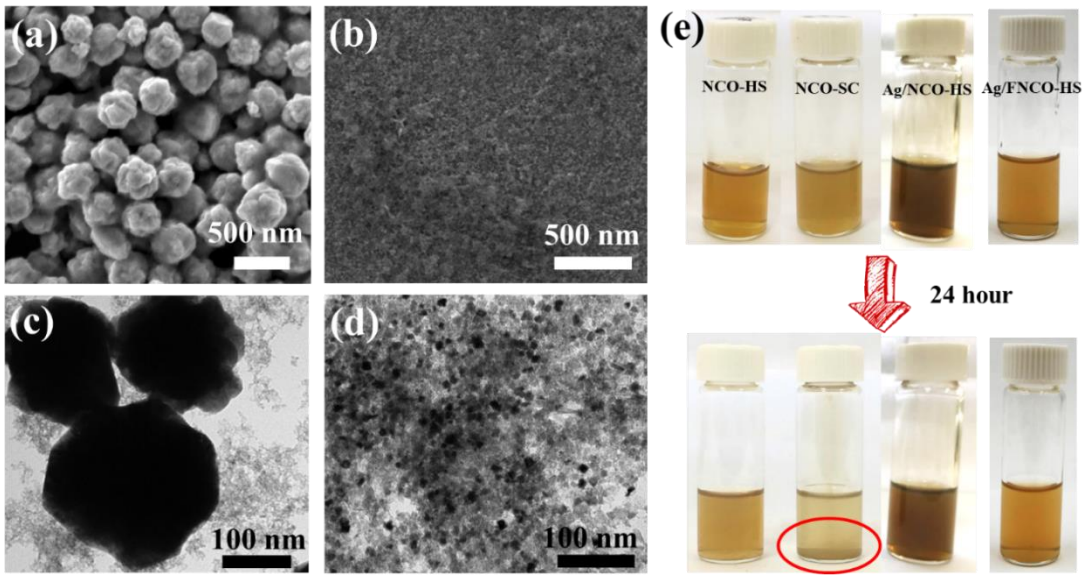

Figure 3. The characterization of control samples and suspension tests. (a) SEM and (c) TEM images of the samples prepared under the oleylamine-free procedure yielding solid core samples (NCO-SC). (b) SEM and (d) TEM images of the samples prepared under TBAOH-free procedure showing nano-flakes instead of spherical morphology. (e) The suspension tests of NCO-HS, NCO-SC, Ag/NCO-HS and Ag/FNCO-HS in a water/IPA solution. After 24-hour aging, all the hollow structure samples remain well suspended, except for NCO-SC (precipitates indicated by the red circle).

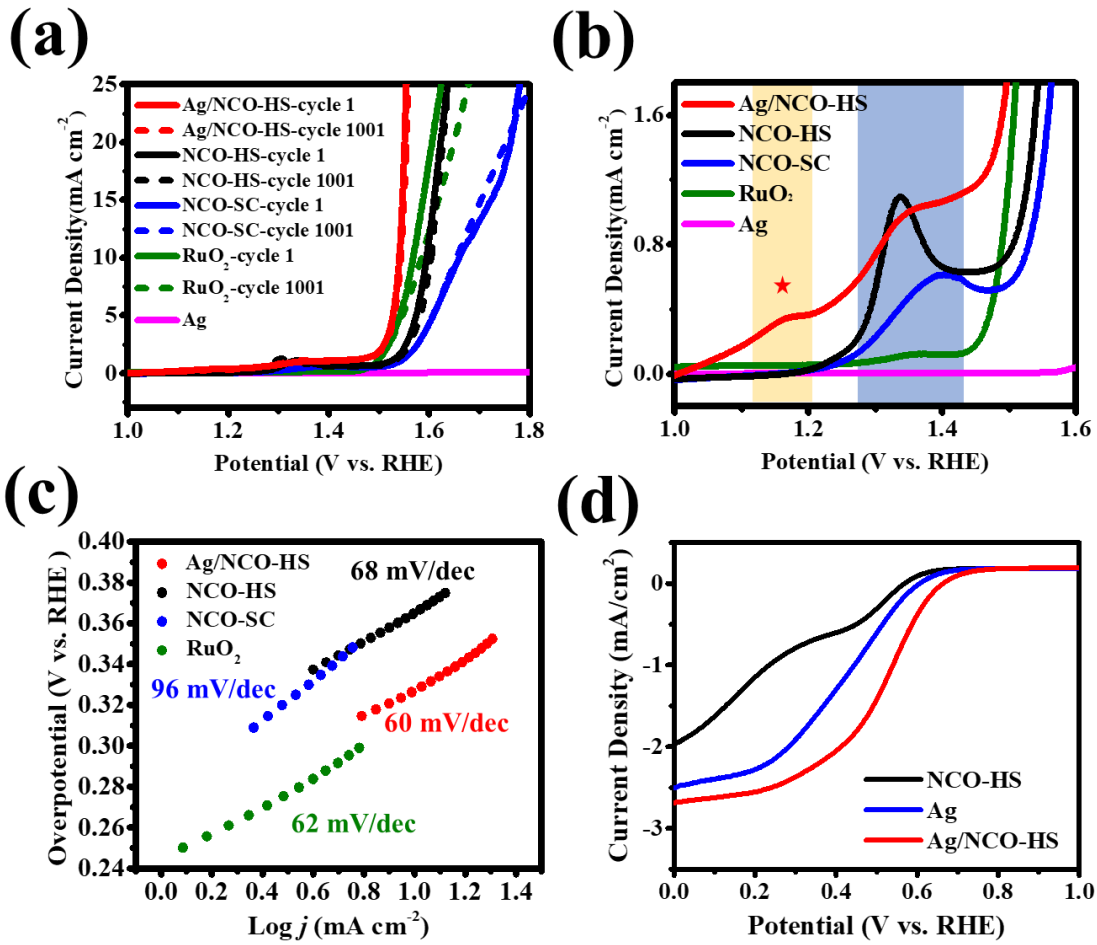

Figure 4. Electrocatalytic performance comparison. (a) The OER LSV curves of the samples in 0.1 M KOH at rotation of 1600 rpm. (b) The magnified OER LSV curves of (a) to reveal the potentials for oxidation number changes of Ni and Co in the electrocatalysts. Two peak regions labeled by yellow and blue correspond to Co and Ni oxidation signals, respectively. (c) The OER Tafel plots of the electrocatalysts. (d) The ORR LSV curves of the samples recorded at 1600 rpm in O_2-saturated 0.1 M KOH (counter electrode: glassy carbon).

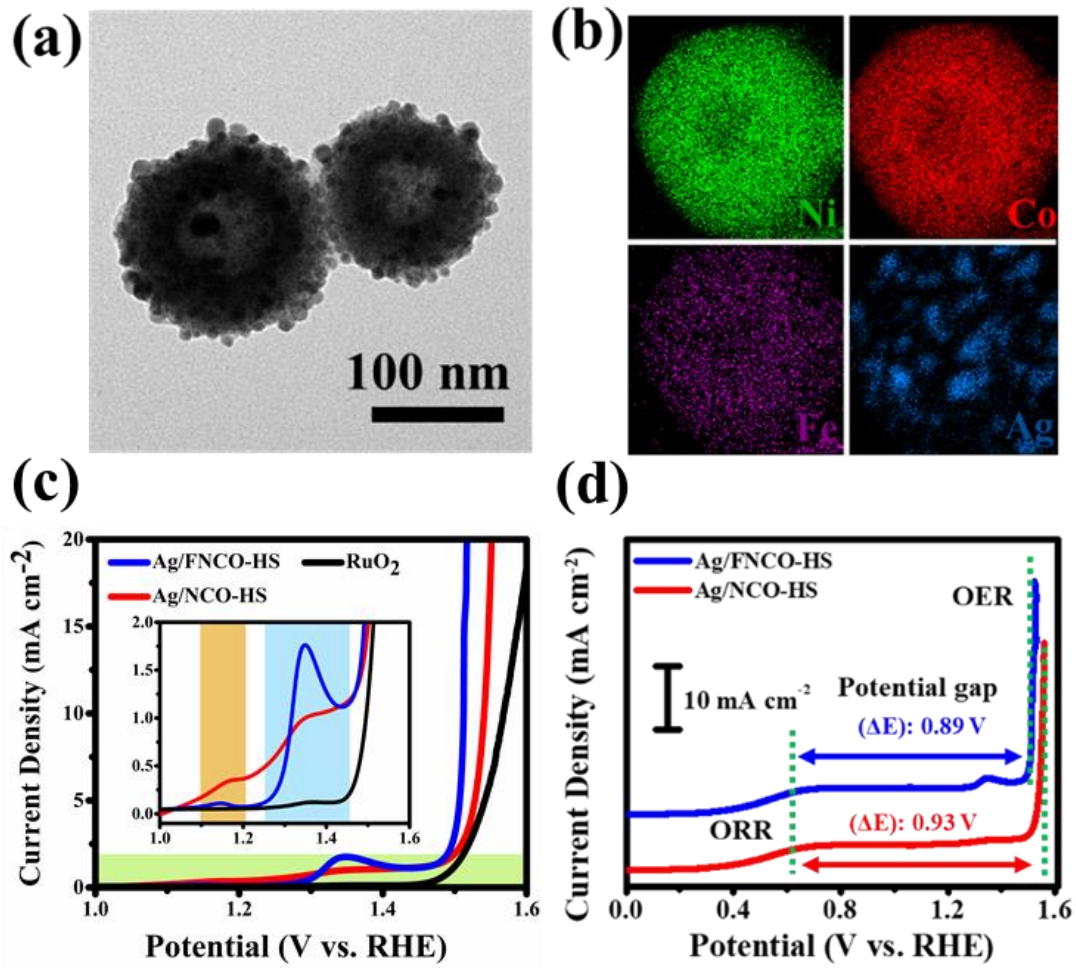

Figure 5. Characterization of Ag-decorated Fe-doped NiO-CoO hollow spheres (Ag/FNCO-HS). (a) TEM images of Ag/FNCO-HS. (b) The EDS mapping of Ni, Co, Fe and Ag of an individual hollow sphere. (c) The OER LSV curves catalyzed by Ag/FNCO-HS in comparison with iron-free Ag/NCO-HS; the inset which magnifies the green region shows the peaks corresponding to Co^{2+} (orange band) and Ni^{2+} (light blue band) oxidation. (d) The ORR and OER bifunctional activities of Ag/FNCO-HS with a potential gap smaller than Ag/NCO-HS by 40 mV.

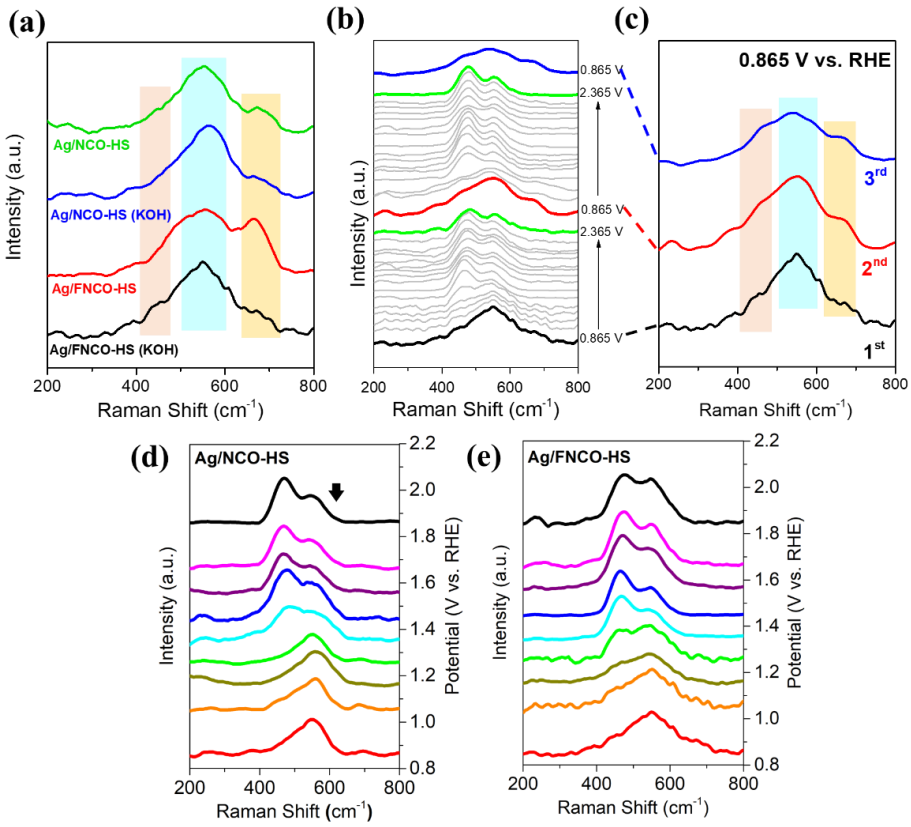

Figure 6. The Raman studies of the electrocatalysts. (a) The comparsion of Ag/NCO-HS and Ag/FNCO-HS in dry and KOH-immersed conditions. (b) The Raman spectra of Ag/FNCO-HS associated with the charge-discharge OER cycles; charging from 0.865 to 2.365 V (black to green) and then return to the rest conditions at 0.865 V immediately (green to red). (c) The comparison of zero charge (0.865 V) curves acquired from (b) connected with the dashed lines. Notation of 1^{st}, 2^{nd}, and 3^{rd} represents the rest conditions between the two successive charge-discharge cycles. The pink, blue, and yellow highlights in (a) and (c) emphasize the Raman shift bands of 450, 550, 670 cm^{-1}, respectively. The operando Raman-coupled electrocatalysis of (d) Ag/NCO-HS and (e) Ag/FNCO-HS during the OER process; the arrow in (d) indicates the shoulder for $Co^{III}OOH$ vibration. The right axes show the potential to which each Raman spectrum was measured.

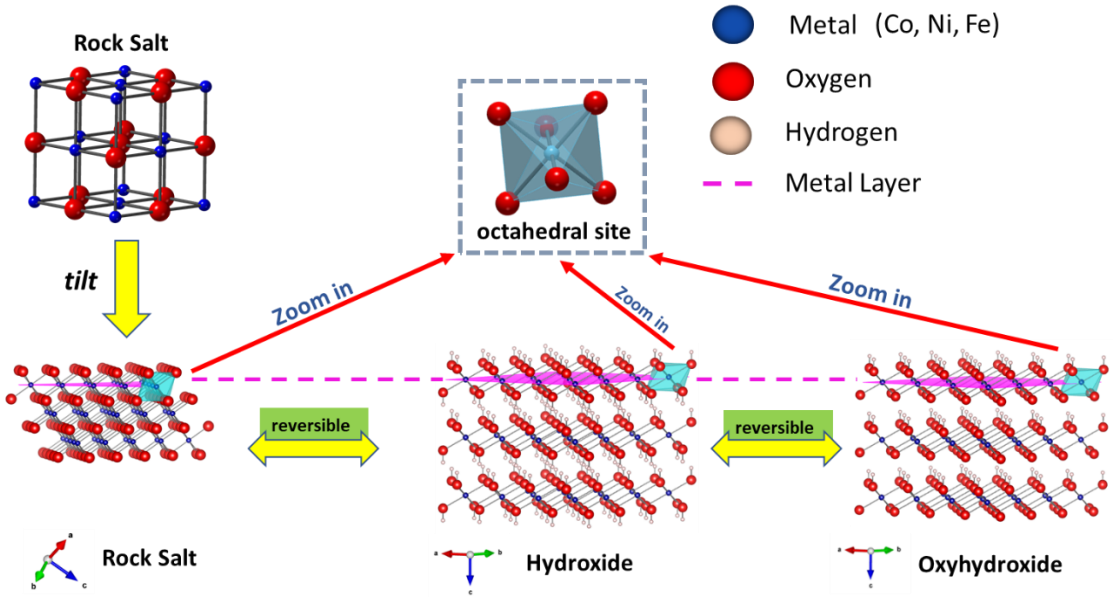

Scheme 2. The illustrated phase transition of rock salt ternary oxides during OER process. The plane of metal cation array is labeled by the pink dash lines along the three phases, showing that no position change or inter-layer migration of the correspnding metal cations occurs upon the phaes transformation. The octahedrally coordinated environments of metals are highlighted in blue, which remains nearly identical in each stage of phase transfromation, supporting the highly reversible local environment from rock salt oxide to oxyhydroxide in OER.

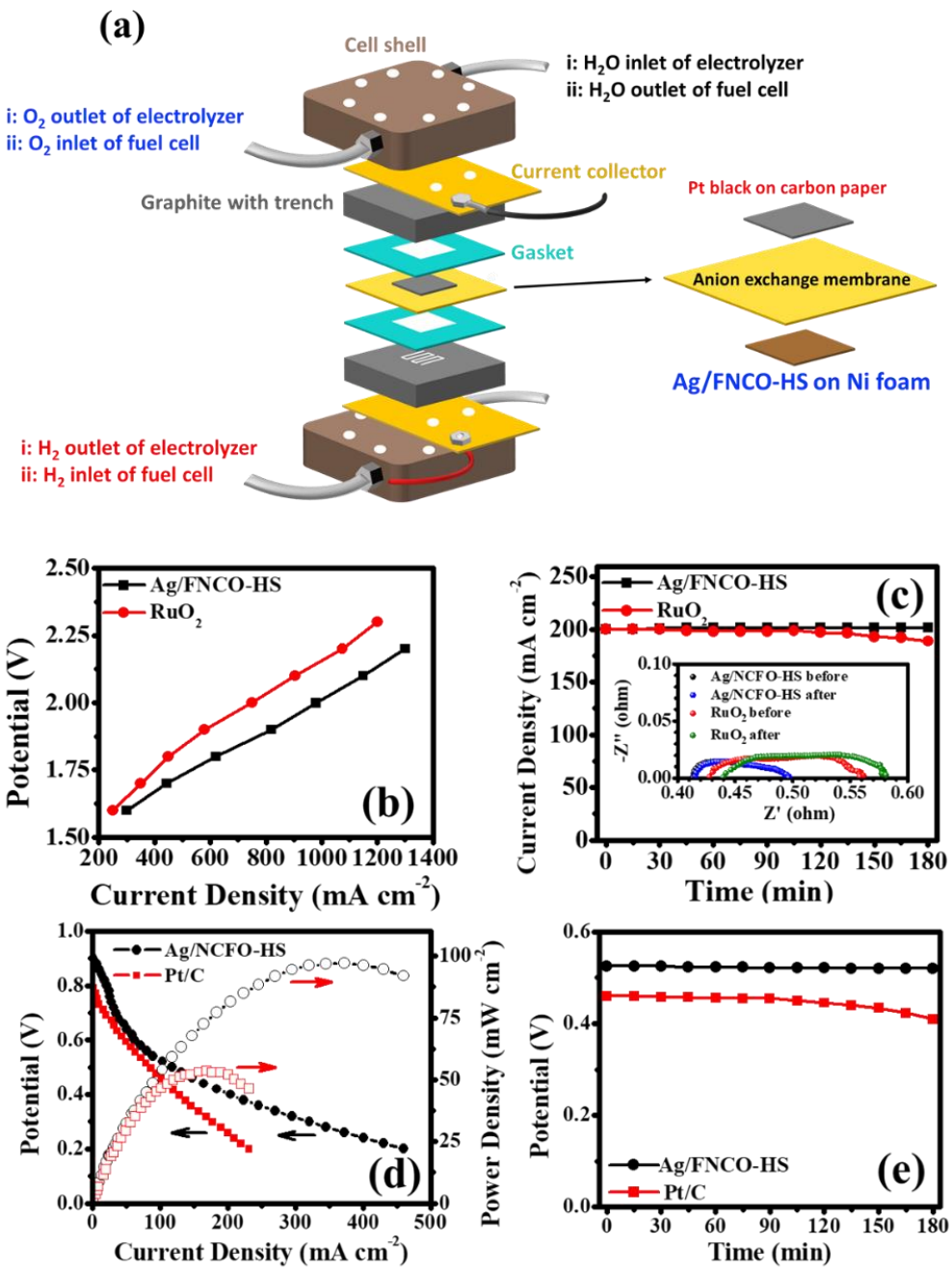

Figure 7. Bifunctional device performance using the Ag/NCO-HS catalyst as compared to the benchmarks. (a) The cell assembly of AEM device where the inlets and outlets for electrolyzer and fuel cell modes are labelled as (i) and (ii), respectively. (b) The electrolyzer mode performance comparison between Ag/FNCO-HS and RuO_2 as alkaline OER

electrocatalysts. (c) The corresponding stability tests of catalysts in (b) at constant potential of 1.50 V, where the inset shows the EIS of the corresponding devices measured before and after the stability tests. (d) The fuel cell mode performance comparison between Ag/FNCO-HS and Pt as the alkaline ORR electrocatalysts. (e) The stability tests of the catalysts in (d) at constant current density of 100 mA cm^{-2}.

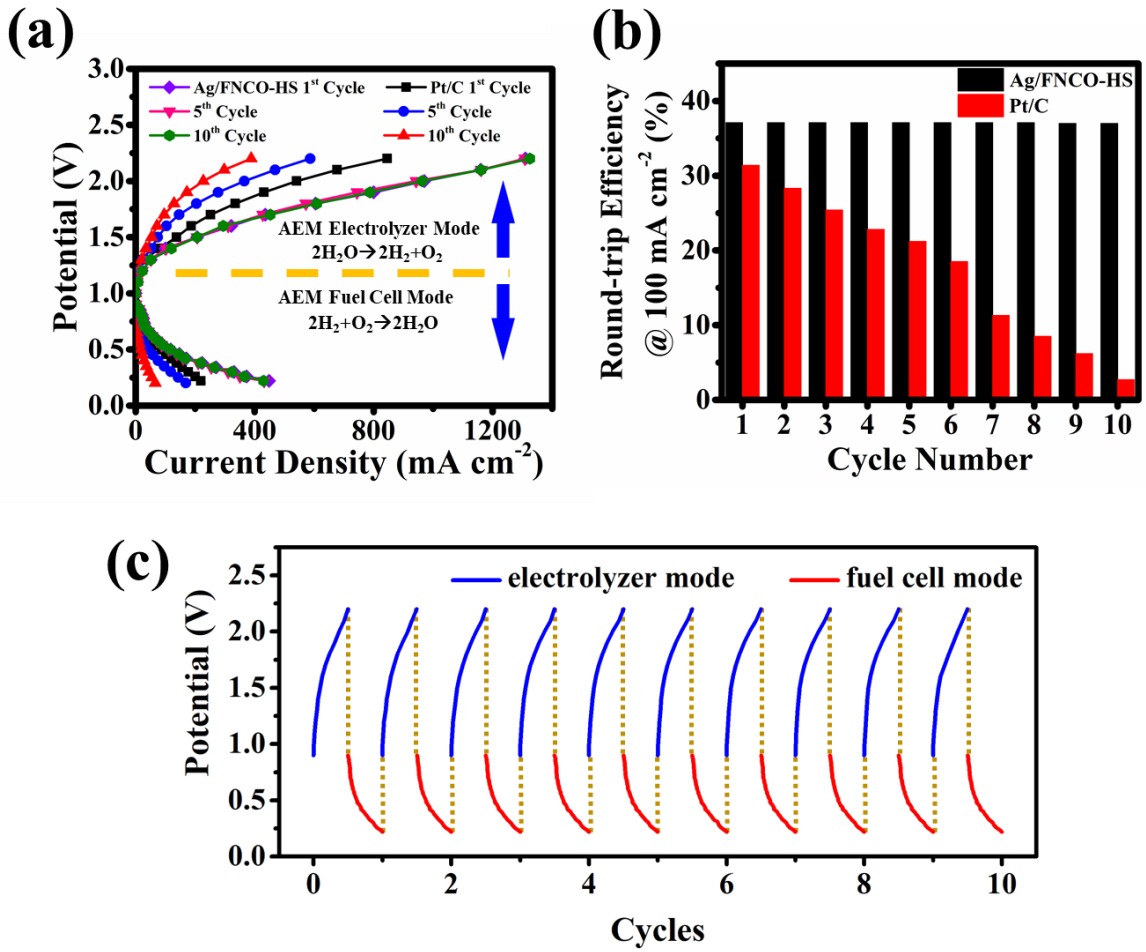

Figure 8. The AEM devices performance comparison between modes of electrolyzer and fuel cell using Ag/FNCO-HS and Pt/C. (a) The polarization curves of the devices measured over 10 cycles, where each cycle includes one electrolyzer test followed by one run of fuel cell mode. (b) The round-trip efficiency (based on Eq. 1) at 100 mA cm^{-2} for ten cycles. The carbon-free Ag/FNCO-HS shows the higher durability than carbon-based Pt/C. (c) Data set of the cycle tests, where the yellow dotted lines indicate the swapping in each cycle. The maximum current density achieved is 1.3 A/cm^2 and 430 mA/cm^2 for the electrolyzer and fuel cell modes, respectively.

REFERENCES

1. Wagner, F. T.; Lakshmanan, B.; Mathias, M. F. Electrochemistry and the Future of the Automobile. *J. Phys. Chem. Lett.* **2010,** *1* (14), 2204-2219.
2. Yang, Z.; Zhang, J.; Kintner-Meyer, M. C. W.; Lu, X.; Choi, D.; Lemmon, J. P.; Liu, J., Electrochemical Energy Storage for Green Grid. *Chem. Rev.* **2011,** *111* (5), 3577-3613.
3. Ng, J. W. D.; Tang, M.; Jaramillo, T. F. A carbon-free, precious-metal-free, high-performance O_2 electrode for regenerative fuel cells and metal–air batteries. *Energy Environ. Sci.* **2014,** *7* (6), 2017-2024.
4. Park, S.; Shao, Y.; Liu, J.; Wang, Y. Oxygen electrocatalysts for water electrolyzers and reversible fuel cells: status and perspective. *Energy Environ. Sci.* **2012,** *5* (11), 9331-9344.
5. Desmond Ng, J. W.; Gorlin, Y.; Hatsukade, T.; Jaramillo, T. F. A Precious-Metal-Free Regenerative Fuel Cell for Storing Renewable Electricity. *Adv. Energy Mater.* **2013,** *3* (12), 1545-1550.
6. Gupta, S.; Zhao, S.; Wang, X. X.; Hwang, S.; Karakalos, S.; Devaguptapu, S. V.; Mukherjee, S.; Su, D.; Xu, H.; Wu, G. Quaternary FeCoNiMn-Based Nanocarbon Electrocatalysts for Bifunctional Oxygen Reduction and Evolution: Promotional Role of Mn Doping in Stabilizing Carbon. *ACS Catal.* **2017,** *7* (12), 8386-8393.
7. Wu, Z.-S.; Yang, S.; Sun, Y.; Parvez, K.; Feng, X.; Müllen, K. 3D Nitrogen-Doped Graphene Aerogel-Supported Fe_3O_4 Nanoparticles as Efficient Electrocatalysts for the Oxygen Reduction Reaction. *J. Am. Chem. Soc.* **2012,** *134* (22), 9082-9085.
8. Kao, W.-Y.; Chen, W.-Q.; Chiu, Y.-H.; Ho, Y.-H.; Chen, C.-H. General Solvent-dependent Strategy toward Enhanced Oxygen Reduction Reaction in Graphene/Metal Oxide Nanohybrids: Effects of Nitrogen-containing Solvent. *Sci. Rep.* **2016,** *6* (1), 37174.
9. Jang, S.-E.; Kim, H. Effect of Water Electrolysis Catalysts on Carbon Corrosion in Polymer Electrolyte Membrane Fuel Cells. *J. Am. Chem. Soc.* **2010,** *132* (42), 14700-14701.
10. Lan, W.-J.; Kuo, C.-C.; Chen, C.-H. Hierarchical nanostructures with unique Y-shaped interconnection networks in manganese substituted cobalt oxides: the enhancement effect on electrochemical sensing performance. *Chem. Commun.* **2013,** *49* (29), 3025-3027.
11. Kuo, C.-C.; Lan, W.-J.; Chen, C.-H. Redox preparation of mixed-valence cobalt manganese oxide nanostructured materials: highly efficient noble metal-free electrocatalysts for sensing hydrogen peroxide. *Nanoscale* **2014,** *6* (1), 334-341.
12. Deng, X.; Öztürk, S.; Weidenthaler, C.; Tüysüz, H. Iron-Induced Activation of Ordered Mesoporous Nickel Cobalt Oxide Electrocatalyst for the Oxygen Evolution Reaction. *ACS Appl. Mater. Interfaces* **2017,** *9* (25), 21225-21233.
13. Kuboon, S.; Hu, Y. H. Study of NiO−CoO and Co_3O_4−Ni_3O_4 Solid Solutions in Multiphase Ni−Co−O Systems. *Ind. Eng. Chem. Res.* **2011,** *50* (4), 2015-2020.
14. Trotochaud, L.; Ranney, J. K.; Williams, K. N.; Boettcher, S. W. Solution-Cast Metal Oxide Thin Film Electrocatalysts for Oxygen Evolution. *J. Am. Chem. Soc.* **2012,** *134* (41), 17253-17261.

15. Sakata, T.; Sakata, K. Change of Oxygen Concentration with Temperature of the Nickel and Cobalt Oxide Solid Solution. *J. Phys. Soc. Jpn.* **1958,** *13* (7), 675-683.
16. Chen, W.-Q.; Chung, M.-C.; Valinton, J. A. A.; Penaloza, D. P.; Chuang, S.-H.; Chen, C.-H. Heterojunctions of silver–iron oxide on graphene for laser-coupled oxygen reduction reactions. *Chem. Commun.* **2018,** *54* (57), 7900-7903.
17. Nørskov, J. K.; Rossmeisl, J.; Logadottir, A.; Lindqvist, L.; Kitchin, J. R.; Bligaard, T.; Jónsson, H. Origin of the Overpotential for Oxygen Reduction at a Fuel-Cell Cathode. *J. Phys. Chem. B* **2004,** *108* (46), 17886-17892.
18. Mohammadkhani, S.; Schaal, E.; Dolatabadi, A.; Moreau, C.; Davis, B.; Guay, D.; Roué, L. Synthesis and thermal stability of (Co,Ni)O solid solutions. *J. Am. Ceram. Soc.* **2019,** *102* (9), 5063-5070.
19. Liyanage, D. R.; Danforth, S. J.; Liu, Y.; Bussell, M. E.; Brock, S. L. Simultaneous Control of Composition, Size, and Morphology in Discrete $Ni_{2-x}Co_xP$ Nanoparticles. *Chem. Mater.* **2015,** *27* (12), 4349-4357.
20. Crystal Ionic Radii of the Elements. In *CRC Handbook of Chemistry and Physics*, 1st Stident ed.; Weast, R.C. Eds.; CRC Press, 1987, p. F-105.
21. Grosvenor, A. P.; Biesinger, M. C.; Smart, R. S. C.; McIntyre, N. S. New interpretations of XPS spectra of nickel metal and oxides. *Surf. Sci.* **2006,** *600* (9), 1771-1779.
22. Thi, T. V.; Rai, A. K.; Gim, J.; Kim, J. High performance of Co-doped NiO nanoparticle anode material for rechargeable lithium ion batteries. *J. Power Sources* **2015,** *292*, 23-30.
23. Zheng, Y.; Zheng, L.; Zhan, Y.; Lin, X.; Zheng, Q.; Wei, K. Ag/ZnO Heterostructure Nanocrystals: Synthesis, Characterization, and Photocatalysis. *Inorg. Chem.* **2007,** *46* (17), 6980-6986.
24. Walton, A. S.; Fester, J.; Bajdich, M.; Arman, M. A.; Osiecki, J.; Knudsen, J.; Vojvodic, A.; Lauritsen, J. V. Interface Controlled Oxidation States in Layered Cobalt Oxide Nanoislands on Gold. *ACS Nano* **2015,** *9* (3), 2445-2453.
25. Hou, Y.; Liu, Y.; Gao, R.; Li, Q.; Guo, H.; Goswami, A.; Zboril, R.; Gawande, M. B.; Zou, X. $Ag@Co_xP$ Core–Shell Heterogeneous Nanoparticles as Efficient Oxygen Evolution Reaction Catalysts. *ACS Catal.* **2017,** *7* (10), 7038-7042.
26. Zhang, Z.; Li, X.; Zhong, C.; Zhao, N.; Deng, Y.; Han, X.; Hu, W. Spontaneous Synthesis of Silver-Nanoparticle-Decorated Transition-Metal Hydroxides for Enhanced Oxygen Evolution Reaction. *Angew. Chem. Int. Ed.* **2020,** *59* (18), 7245-7250.
27. Lu, J.; Zhou, W.; Wang, L.; Jia, J.; Ke, Y.; Yang, L.; Zhou, K.; Liu, X.; Tang, Z.; Li, L.; Chen, S. Core–Shell Nanocomposites Based on Gold Nanoparticle@Zinc–Iron-Embedded Porous Carbons Derived from Metal–Organic Frameworks as Efficient Dual Catalysts for Oxygen Reduction and Hydrogen Evolution Reactions. *ACS Catal.* **2016,** *6* (2), 1045-1053.
28. He, H.; Chen, J.; Zhang, D.; Li, F.; Chen, X.; Chen, Y.; Bian, L.; Wang, Q.; Duan, P.; Wen, Z.; Lv, X. Modulating the Electrocatalytic Performance of Palladium with the Electronic Metal–Support Interaction: A Case Study on Oxygen Evolution Reaction. *ACS Catal.* **2018,** *8* (7), 6617-6626.
29. Chala, S. A.; Tsai, M.-C.; Su, W.-N.; Ibrahim, K. B.; Thirumalraj, B.; Chan, T.-S.; Lee, J.-F.; Dai, H.; Hwang, B.-J. Hierarchical 3D Architectured Ag Nanowires Shelled

with NiMn-Layered Double Hydroxide as an Efficient Bifunctional Oxygen Electrocatalyst. *ACS Nano* **2020,** *14* (2), 1770-1782.
30. Chala, S. A.; Tsai, M.-C.; Su, W.-N.; Ibrahim, K. B.; Duma, A. D.; Yeh, M.-H.; Wen, C.-Y.; Yu, C.-H.; Chan, T.-S.; Dai, H.; Hwang, B.-J. Site Activity and Population Engineering of NiRu-Layered Double Hydroxide Nanosheets Decorated with Silver Nanoparticles for Oxygen Evolution and Reduction Reactions. *ACS Catal.* **2019,** *9* (1), 117-129.
31. Mandal Goswami, M. Synthesis of Micelles Guided Magnetite (Fe_3O_4) Hollow Spheres and their application for AC Magnetic Field Responsive Drug Release. *Sci. Rep.* **2016,** *6* (1), 35721.
32. Xu, Y.; Bian, W.; Wu, J.; Tian, J.-H.; Yang, R. Preparation and electrocatalytic activity of 3D hierarchical porous spinel $CoFe_2O_4$ hollow nanospheres as efficient catalyst for Oxygen Reduction Reaction and Oxygen Evolution Reaction. *Electrochim. Acta* **2015,** *151*, 276-283.
33. Zeng, L.; Sun, K.; Chen, Y.; Liu, Z.; Chen, Y.; Pan, Y.; Zhao, R.; Liu, Y.; Liu, C. Neutral-pH overall water splitting catalyzed efficiently by a hollow and porous structured ternary nickel sulfoselenide electrocatalyst. *J. Mater. Chem. A* **2019,** *7* (28), 16793-16802.
34. Moysiadou, A.; Hu, X. Stability profiles of transition metal oxides in the oxygen evolution reaction in alkaline medium. *J. Mater. Chem. A* **2019,** *7* (45), 25865-25877.
35. Burke, M. S.; Kast, M. G.; Trotochaud, L.; Smith, A. M.; Boettcher, S. W. Cobalt–Iron (Oxy)hydroxide Oxygen Evolution Electrocatalysts: The Role of Structure and Composition on Activity, Stability, and Mechanism. *J. Am. Chem. Soc.* **2015,** *137* (10), 3638-3648.
36. Vishnu Prataap, R. K.; Mohan, S. Electrodeposited-hydroxide surface-covered porous nickel–cobalt alloy electrodes for efficient oxygen evolution reaction. *Chem. Commun.* **2017,** *53* (23), 3365-3368.
37. Smith, R. D. L.; Prévot, M. S.; Fagan, R. D.; Trudel, S.; Berlinguette, C. P. Water Oxidation Catalysis: Electrocatalytic Response to Metal Stoichiometry in Amorphous Metal Oxide Films Containing Iron, Cobalt, and Nickel. *J. Am. Chem. Soc.* **2013,** *135* (31), 11580-11586.
38. Lv, X.; Zhu, Y.; Jiang, H.; Yang, X.; Liu, Y.; Su, Y.; Huang, J.; Yao, Y.; Li, C. Hollow mesoporous $NiCo_2O_4$ nanocages as efficient electrocatalysts for oxygen evolution reaction. *Dalton Trans.* **2015,** *44* (9), 4148-4154.
39. Tan, Y.; Xu, C.; Chen, G.; Fang, X.; Zheng, N.; Xie, Q. Facile Synthesis of Manganese-Oxide-Containing Mesoporous Nitrogen-Doped Carbon for Efficient Oxygen Reduction. *Adv. Funct. Mater.* **2012,** *22* (21), 4584-4591.
40. Men, B.; Sun, Y.; Tang, Y.; Zhang, L.; Chen, Y.; Wan, P.; Pan, J. Highly Dispersed Ag-Functionalized Graphene Electrocatalyst for Oxygen Reduction Reaction in Energy-Saving Electrolysis of Sodium Carbonate. *Ind. Eng. Chem. Res.* **2015,** *54* (30), 7415-7422.
41. Tamaki, T.; Yamauchi, A.; Ito, T.; Ohashi, H.; Yamaguchi, T. The Effect of Methanol Crossover on the Cathode Overpotential of DMFCs. *Fuel Cells* **2011,** *11* (3), 394-403.
42. Gong, L.; Chng, X. Y. E.; Du, Y.; Xi, S.; Yeo, B. S. Enhanced Catalysis of the Electrochemical Oxygen Evolution Reaction by Iron(III) Ions Adsorbed on Amorphous Cobalt Oxide. *ACS Catal.* **2018,** *8* (2), 807-814.

43. Stevens, M. B.; Trang, C. D. M.; Enman, L. J.; Deng, J.; Boettcher, S. W. Reactive Fe-Sites in Ni/Fe (Oxy)hydroxide Are Responsible for Exceptional Oxygen Electrocatalysis Activity. *J. Am. Chem. Soc.* **2017,** *139* (33), 11361-11364.
44. Cai, Z.; Zhou, D.; Wang, M.; Bak, S.-M.; Wu, Y.; Wu, Z.; Tian, Y.; Xiong, X.; Li, Y.; Liu, W.; Siahrostami, S.; Kuang, Y.; Yang, X.-Q.; Duan, H.; Feng, Z.; Wang, H.; Sun, X. Introducing Fe^{2+} into Nickel–Iron Layered Double Hydroxide: Local Structure Modulated Water Oxidation Activity. *Angew. Chem. Int. Ed.* **2018,** *57* (30), 9392-9396.
45. Ahmed, M. S.; Choi, B.; Kim, Y.-B. Development of Highly Active Bifunctional Electrocatalyst Using Co_3O_4 on Carbon Nanotubes for Oxygen Reduction and Oxygen Evolution. *Sci. Rep.* **2018,** *8* (1), 2543.
46. Li, S.; Cheng, C.; Zhao, X.; Schmidt, J.; Thomas, A. Active Salt/Silica-Templated 2D Mesoporous FeCo-N_x-Carbon as Bifunctional Oxygen Electrodes for Zinc–Air Batteries. *Angew. Chem. Int. Ed.* **2018,** *57* (7), 1856-1862.
47. Rivas-Murias, B.; Salgueiriño, V. Thermodynamic CoO–Co_3O_4 crossover using Raman spectroscopy in magnetic octahedron-shaped nanocrystals. *J. Raman Spectrosc.* **2017,** *48* (6), 837-841.
48. Yang, J.; Liu, H.; Martens, W. N.; Frost, R. L. Synthesis and Characterization of Cobalt Hydroxide, Cobalt Oxyhydroxide, and Cobalt Oxide Nanodiscs. *J. Phys. Chem. C* **2010,** *114* (1), 111-119.
49. Wang, X.; Liu, Y.; Zhang, T.; Luo, Y.; Lan, Z.; Zhang, K.; Zuo, J.; Jiang, L.; Wang, R. Geometrical-Site-Dependent Catalytic Activity of Ordered Mesoporous Co-Based Spinel for Benzene Oxidation: In Situ DRIFTS Study Coupled with Raman and XAFS Spectroscopy. *ACS Catal.* **2017,** *7* (3), 1626-1636.
50. Wu, Z.; Zou, Z.; Huang, J.; Gao, F. Fe-doped NiO mesoporous nanosheets array for highly efficient overall water splitting. *J. Catal.* **2018,** *358*, 243-252.
51. Rojas, E.; Delgado, J. J.; Guerrero-Pérez, M. O.; Bañares, M. A. Performance of NiO and Ni–Nb–O active phases during the ethane ammoxidation into acetonitrile. *Catal. Sci. Technol.* **2013,** *3* (12), 3173-3182.
52. Del Pilar-Albaladejo, J.; Dutta, P. K. Topotactic Transformation of Zeolite Supported Cobalt(II) Hydroxide to Oxide and Comparison of Photocatalytic Oxygen Evolution. *ACS Catal.* **2014,** *4* (1), 9-15.
53. Balram, A.; Zhang, H.; Santhanagopalan, S. Enhanced Oxygen Evolution Reaction Electrocatalysis via Electrodeposited Amorphous α-Phase Nickel-Cobalt Hydroxide Nanodendrite Forests. *ACS Appl. Mater. Interfaces* **2017,** *9* (34), 28355-28365.
54. Thanos, I. C. G. In situ Raman and other studies of electrochemically oxidized iron and iron-9% chromium alloy. *Electrochim. Acta* **1986,** *31* (7), 811-820.
55. Lo, Y. L.; Hwang, B. J. In Situ Raman Studies on Cathodically Deposited Nickel Hydroxide Films and Electroless Ni−P Electrodes in 1 M KOH Solution. *Langmuir* **1998,** *14* (4), 944-950.
56. Zheng, W.; Liu, M.; Lee, L. Y. S. Electrochemical Instability of Metal–Organic Frameworks: In Situ Spectroelectrochemical Investigation of the Real Active Sites. *ACS Catal.* **2020,** *10* (1), 81-92.
57. Louie, M. W.; Bell, A. T. An Investigation of Thin-Film Ni–Fe Oxide Catalysts for the Electrochemical Evolution of Oxygen. *J. Am. Chem. Soc.* **2013,** *135* (33), 12329-12337.

58. Trześniewski, B. J.; Diaz-Morales, O.; Vermaas, D. A.; Longo, A.; Bras, W.; Koper, M. T. M.; Smith, W. A. In Situ Observation of Active Oxygen Species in Fe-Containing Ni-Based Oxygen Evolution Catalysts: The Effect of pH on Electrochemical Activity. *J. Am. Chem. Soc.* **2015,** *137* (48), 15112-15121.
59. Moysiadou, A.; Lee, S.; Hsu, C.-S.; Chen, H. M.; Hu, X. Mechanism of Oxygen Evolution Catalyzed by Cobalt Oxyhydroxide: Cobalt Superoxide Species as a Key Intermediate and Dioxygen Release as a Rate-Determining Step. *J. Am. Chem. Soc.* **2020,** *142* (27), 11901-11914.
60. Chen, C.-H.; Njagi, E. C.; Chen, S.-Y.; Horvath, D. T.; Xu, L.; Morey, A.; Mackin, C.; Joesten, R.; Suib, S. L. Structural Distortion of Molybdenum-Doped Manganese Oxide Octahedral Molecular Sieves for Enhanced Catalytic Performance. *Inorg. Chem.* **2015,** *54* (21), 10163-10171.
61. Niu, S.; Sun, Y.; Sun, G.; Rakov, D.; Li, Y.; Ma, Y.; Chu, J.; Xu, P. Stepwise Electrochemical Construction of FeOOH/$Ni(OH)_2$ on Ni Foam for Enhanced Electrocatalytic Oxygen Evolution. *ACS Appl. Energy. Mater.* **2019,** *2* (5), 3927-3935.
62. Xu, D.; Stevens, M. B.; Cosby, M. R.; Oener, S. Z.; Smith, A. M.; Enman, L. J.; Ayers, K. E.; Capuano, C. B.; Renner, J. N.; Danilovic, N.; Li, Y.; Wang, H.; Zhang, Q.; Boettcher, S. W. Earth-Abundant Oxygen Electrocatalysts for Alkaline Anion-Exchange-Membrane Water Electrolysis: Effects of Catalyst Conductivity and Comparison with Performance in Three-Electrode Cells. *ACS Catal.* **2019,** *9* (1), 7-15.
63. Parrondo, J.; George, M.; Capuano, C.; Ayers, K. E.; Ramani, V. Pyrochlore electrocatalysts for efficient alkaline water electrolysis. *J. Mater. Chem. A* **2015,** *3* (20), 10819-10828.
64. Cifrain, M.; Kordesch, K. V. Advances, aging mechanism and lifetime in AFCs with circulating electrolytes. *J. Power Sources* **2004,** *127* (1), 234-242.
65. Fujiwara, N.; Yao, M.; Siroma, Z.; Senoh, H.; Ioroi, T.; Yasuda, K. Reversible air electrodes integrated with an anion-exchange membrane for secondary air batteries. *J. Power Sources* **2011,** *196* (2), 808-813.
66. Liu, L.; Chu, X.; Liao, J.; Huang, Y.; Li, Y.; Ge, Z.; Hickner, M. A.; Li, N. Tuning the properties of poly(2,6-dimethyl-1,4-phenylene oxide) anion exchange membranes and their performance in H_2/O_2 fuel cells. *Energy Environ. Sci.* **2018,** *11* (2), 435-446.
67. Sapountzi, F. M.; Gracia, J. M.; Weststrate, C. J.; Fredriksson, H. O. A.; Niemantsverdriet, J. W. Electrocatalysts for the generation of hydrogen, oxygen and synthesis gas. *Progr. Energy Combust. Sci.* **2017,** *58*, 1-35.
68. Huang, K. An Active and Robust Bifunctional Oxygen Electrocatalyst through Carbon-Free Hierarchical Functionalization. *Angew. Chem. Int. Ed.* **2017,** *56* (42), 12826-12827.

TABLE OF CONTENTS